



Effects of a hybrid post-treatment on microstructure and mechanical properties of cold sprayed AA7050 deposits

Chengxin Liu ^a, Xingrong Chu ^{a,*}, Naijiang Wang ^a, Jun Gao ^a, Liang Chen ^b

^a Associated Engineering Research Center of Mechanics and Mechatronic Equipment, Shandong University, Weihai 264209, PR China

^b Key Laboratory for Liquid-Solid Structural Evolution and Processing of Materials (Ministry of Education), Shandong University, Jinan, Shandong 250061, PR China

ARTICLE INFO

Keywords:

Cold spray
Additive manufacturing
Heat treatments
Microstructure
Mechanical properties
Aluminum alloy

ABSTRACT

Cold spray additive manufacturing (CSAM) technology is a promising and efficient method for preparing high-strength aluminum alloy components. In this work, AA7050 deposits were prepared by high-pressure cold spraying, and a hybrid post-treatment (i.e., annealing + hot compression + solid solution and aging) was proposed to improve the mechanical properties of the deposits. The results of the study indicated that the annealing alone was insufficient to eliminate all defects within the AA7050 deposits. After annealing, the porosity of the material decreased from 2.34% to 1.62%. The subsequent hot compression and aging treatment promoted the precipitation of strengthening phases and homogenized the microstructure, reducing the porosity of the AA7050 deposits to 0.18%. As a result, the mechanical properties of the materials further improved. The ultimate tensile strength of the CSAMed AA7050 after aging treatment reached 557.7 MPa, which was 337.4% and 149.3% higher than that of the as-sprayed and annealed materials, respectively. Furthermore, fracture surfaces analysis indicated that the fracture mechanism of the specimens changed from brittle to ductile mode after the hybrid post-treatment.

1. Introduction

Cold spray technology is an emerging solid-state powder deposition technology. During the cold spraying, the feedstock particles are accelerated to high velocities by pressurized gases and then make impact with the substrates or deposited particles. The severe plastic deformation and adiabatic shear that occur upon impact leads to mechanical interlocking and metallurgical bonding of the particles with the impact sites [1–3]. The deposition of particles relies primarily on the kinetic energy of the particles rather than on thermal energy. Thus, the oxidation and phase transformation of the particles are effectively avoided, and the properties of the feedstock particles can be retained in the deposits [4]. Currently, cold spray technology has been widely researched in the field of coatings, such as protective coatings for substrate [5,6] and functional coatings with specific properties [7,8]. The unique characteristics of cold spraying technology, including high deposition efficiency and unlimited deposition thickness facilitate its gradual expansion from coating preparation to additive manufacturing, leading to the development of cold spray additive manufacturing (CSAM) technology [9,10].

Metal additive manufacturing technologies based on heat input have been widely studied, such as wire arc additive manufacturing

technology using welding wire as feedstock, as well as powder-based electron beam additive manufacturing technology and laser additive manufacturing technology [11–13]. Nevertheless, excessive heat input tends to generate micro-defects within the deposits, which can be effectively avoided by the CSAM technology [14]. As a result, CSAM technology offers unique advantages in the preparation process of highly reflective and thermally sensitive materials, such as copper, aluminum, and their alloys. However, the mechanical properties of CSAMed deposits, especially the ductility, are significantly constrained by the predominantly mechanical interlocking mode of bonding between particles within the materials, which limits the application scope of CSAM technology [15]. To address this issue, researchers incorporate the post-treatment of deposits into the scope of CSAM technology to achieve efficient preparation of materials with desired properties.

At present, the most typical post-treatment of CSAMed materials is annealing treatment, which could play a role in repairing the microstructure and alleviating the residual stresses in the deposits. Huang et al. [16] performed annealing treatment on the prepared pure Cu deposits, and the tensile strength of the treated samples increased significantly. Wu et al. [17] carried out heat treatment of CSAMed Inconel 625 materials at 900°C. The results showed that the inter-particle bonding

* Corresponding author.

E-mail address: xrchu@sdu.edu.cn (X. Chu).

state was improved and the material regained plasticity along with the increase in strength. Similarly, Fan et al. [18] demonstrated that the annealing treatment helps balance the strength and plasticity of the CSAMED CoCrFeNi high-entropy alloy. As the internal defects of the material were continuously repaired during the annealing process, the material tension-compression asymmetry was reduced. In addition, the results of Ayan et al. [19] and Deepika et al. [20] showed that reasonable annealing treatment could alleviate residual stresses inside deposits while repairing the microstructure of the cold sprayed deposits. The above findings demonstrate that the annealing treatment could heal most of the particle interfaces as well as repair minor defects within the as-sprayed materials. Nevertheless, it is difficult to further enhance the material densification and optimize the inter-particle bonding state by simple annealing treatment. Therefore, introducing thermo-mechanical coupling treatment is necessary to further improve the microstructure and thus enhance the mechanical properties of CSAMED materials. For instance, Ren et al. [21] proposed a method for treating CSAMED Al deposits by hot forging. The results showed that after the treatment, all micro-defects of the deposits were effectively repaired, and the mechanical properties were significantly improved. Moreover, Ye et al. [22] investigated the effects of conventional heat treatment and hot rolling on the microstructure and properties of CSAMED Cu deposits, and found that the properties of the materials after hot rolling were significantly improved than that after conventional heat treatment.

Furthermore, for heat-treatable aluminum alloys prepared by CSAM technology, solid solution-aging treatment can effectively achieve the desired combination of strength and plasticity [23–25]. However, in the current study, the CSAMED materials were mostly in the untreated or annealed state prior to solid solution and aging treatments. In such cases, micro-defects may persist within the materials even after aging treatment. These defects could act as potential nucleation sites for cracks under stress, thereby compromising the mechanical properties of the materials. Consequently, it is necessary to introduce thermo-mechanical coupling treatment before aging to ensure the elimination of obvious defects within the materials. Moreover, pre-deformation could also facilitate the precipitation and homogeneous distribution of precipitated phases in the subsequent aging process [26], which could contribute to further exploiting the performance potential of CSAMED materials.

AA7050 exhibits high specific strength and corrosion resistance [27–31]. At the same time, the AA7xxx series alloys are widely used in the manufacture of aerospace parts requiring high strength [32,33]. Therefore, the primary aim of this study is to improve the microstructure and mechanical properties of CSAMED AA7050 with a hybrid post-treatment process. In this work, the microstructure evolution of CSAMED AA7050 during the hybrid post-treatment process was investigated. Meanwhile, Vickers microhardness tests and tensile tests were conducted on the materials in different states to evaluate the changes in mechanical properties of AA7050, and the fracture surfaces of the tensile specimens were also analyzed.

2. Materials and methods

2.1. Materials

AA7050 bulk materials were prepared on commercial AA6061 sheet. The chemical element contents of the feedstock powders and AA6061 sheets are detailed in Table 1 and Table 2, respectively. Fig. 1 shows the morphologies of gas-atomized spherical AA7050 feedstock powders (Shanghai buwei applied materials technology Co., Ltd.), which had average diameters of approximately 48 μm.

Table 1

Chemical composition of AA7050 powders (wt%).

	Cu	Si	Mg	Fe	Cr	Zn	Mn	Al	Others
AA7050	2.262	0.085	2.210	0.093	0.024	5.828	0.080	89.010	0.050

Table 2

Chemical composition of AA6061 sheets (wt%).

	Cu	Si	Mg	Fe	Cr	Al
AA6061	0.24	0.62	1.01	0.42	0.11	Bal.

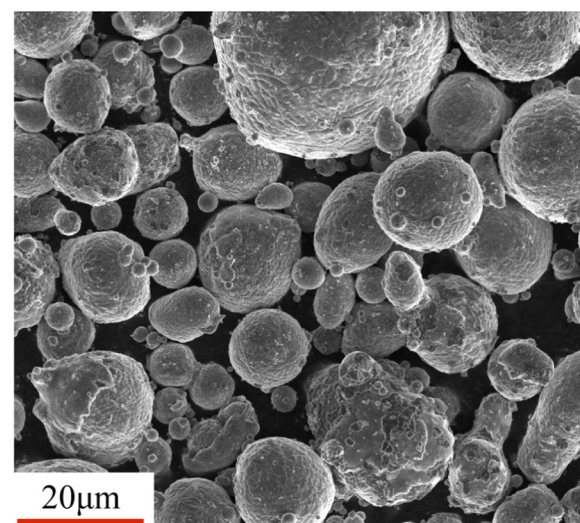


Fig. 1. Morphologies of AA7050 feedstock powders.

2.2. Preparation of AA7050 deposits

The AA7050 bulk materials were prepared using a commercial cold spraying experimental platform (PCS-1000, Plasma Giken, Japan). During the cold spraying, the gun movement was controlled by an industrial robot, following a Z-shaped path and repeating the movement. The speed of the gun movement, the distance between the nozzle and the substrates, and the distance between each pass were 25 mm/s, 25 mm, and 3.5 mm, respectively. N₂ at 500°C and 5 MPa was used as the working gas. Upon completion of the spraying, the dimensions of the prepared AA7050 bulk materials were approximately 100 mm × 100 mm × 5 mm.

2.3. Hybrid post-treatment method

The samples were separated from the CSAMED AA7050 materials by electric discharge wire cutting before post-treatment. First, the samples were annealed at 470°C for 3 hours in a muffle furnace and cooled to room temperature within the furnace. Subsequently, the samples were heated to 470°C and held for 15 minutes, and then compressed along the impact direction at a rate of 1 mm/min, achieving 30% (1.5 mm) and 50% (2.5 mm) reduction, respectively. Finally, the samples with 50% reduction were subjected to solution treatment at 470°C for 2 hours and artificial aging after water quenching. Artificial aging was performed in the oil bath furnace at 160°C for 0, 6, 12, and 24 hours. Table 3 and Fig. 2 summarizes the details of the hybrid post-treatment at different stages.

2.4. Microstructure characterization

The morphologies of the feedstock powders and the fracture surfaces

Table 3

The hybrid post-treatment parameters of CSAMed AA7050 materials.

Sample	Annealing	Hot compression	Solution	Aging
As sprayed	-	-	-	-
HT	470°C/3 h	-	-	-
C-30	470°C/3 h	30% reduction	-	-
C-50	470°C/3 h	50% reduction	-	-
W	470°C/3 h	50% reduction	470°C/2 h	-
A-6	470°C/3 h	50% reduction	470°C/2 h	160°C/6 h
A-12	470°C/3 h	50% reduction	470°C/2 h	160°C/12 h
A-24	470°C/3 h	50% reduction	470°C/2 h	160°C/24 h

of the tensile specimens were analyzed in secondary electron mode using a scanning electron microscope (SEM, Nova Nano SEM 450, USA) equipped with an electron backscatter diffraction (EBSD) analysis system at an accelerating voltage of 10 kV. To examine the microstructure evolution of AA7050 at different treatment stages, the samples were analyzed using a laser confocal microscope (VK-X1000 3D, Japan). The secondary phase evolution in the samples was analyzed in backscattered electron (BSE) mode using an energy dispersive spectrometer (EDS) of SEM (Tescan vega compact, Czech) at 25 keV energy. Based on the cross-section of the samples after mechanical polishing, ImageJ software was utilized to assess the change in porosity of the samples. In addition, the samples were etched with Keller's reagent (95 mL H₂O, 1 mL HF, 1.5 mL HCl, and 2.5 mL HNO₃) for 10–20 seconds to examine the metallographic structure. Before EBSD analysis, the polished samples were treated using an Ilion II Model 697 argon-ion polisher. The step size, accelerating voltage, and sample tilt angle during EBSD testing were 0.2 μm, 20 kV, and 70°, respectively. The data obtained from the EBSD tests were analyzed using Oxford Instrument Channel 5 software. Furthermore, the detailed microstructure of CSAMed AA7050 deposits was analyzed using transmission electron microscope (TEM, FEI Talos

F200X, USA) with an accelerating voltage of 200 kV. Before TEM analysis, the samples were mechanically thinned to about 70 μm and then thinned in a mixed solution of 5% perchloric acid and 95% ethanol using a twin-jet electropolishing device (MTP-1A, China) at –30 °C.

2.5. Mechanical properties characterization

As shown in Fig. 2, the dog-bone shaped tensile specimens were separated from deposits. The tensile tests were conducted on an MTS universal tensile test platform at a tensile speed of 0.05 mm/min, which corresponded to a strain rate of about $1.04 \times 10^{-4} \text{ s}^{-1}$, and each test was repeated three times. The microhardness was evaluated using an MHV-1000Z Vickers microhardness tester, with a test load of 0.98 N for 20 seconds. To ensure the reliability of the results, the average microhardness of the five points on the cross-section was calculated as the microhardness of the samples.

3. Results and discussion

3.1. Microstructure

The cross-section microstructures of AA7050 samples in different states after polishing and the corresponding porosities are shown in Fig. 3. First, Fig. 3(a) reveals that the as-sprayed samples had dense microstructures. However, micro-defects were present among some particles due to insufficient deformation, resulting in porosities of approximately 2.34%. Then, most of the microscopic defects were effectively repaired by atomic diffusion after the annealing treatment, but some minor defects remained in the HT samples. Fig. 3(c) and (d) indicates that hot compression further improved the microstructures of the AA7050 samples, and the porosities were reduced with increased compression. After 50% reduction, the porosities of the C-50 samples

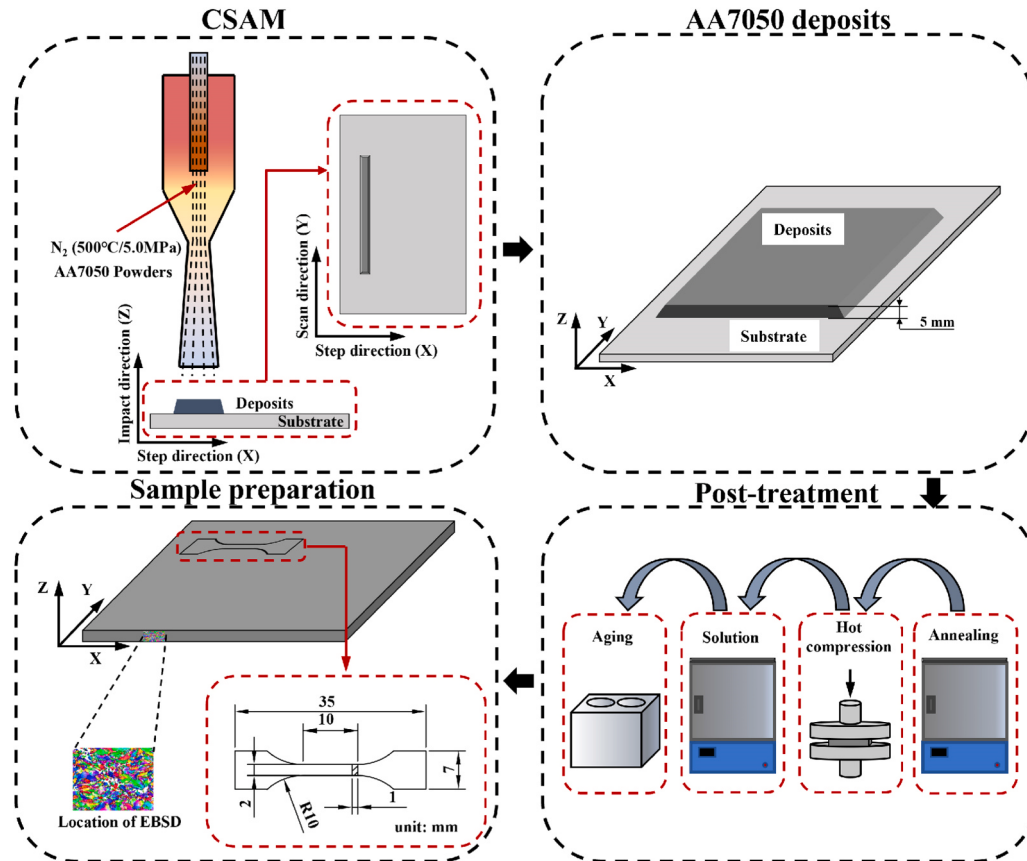


Fig. 2. The main procedures of post-treatment experiments of CSAMed AA7050 materials.

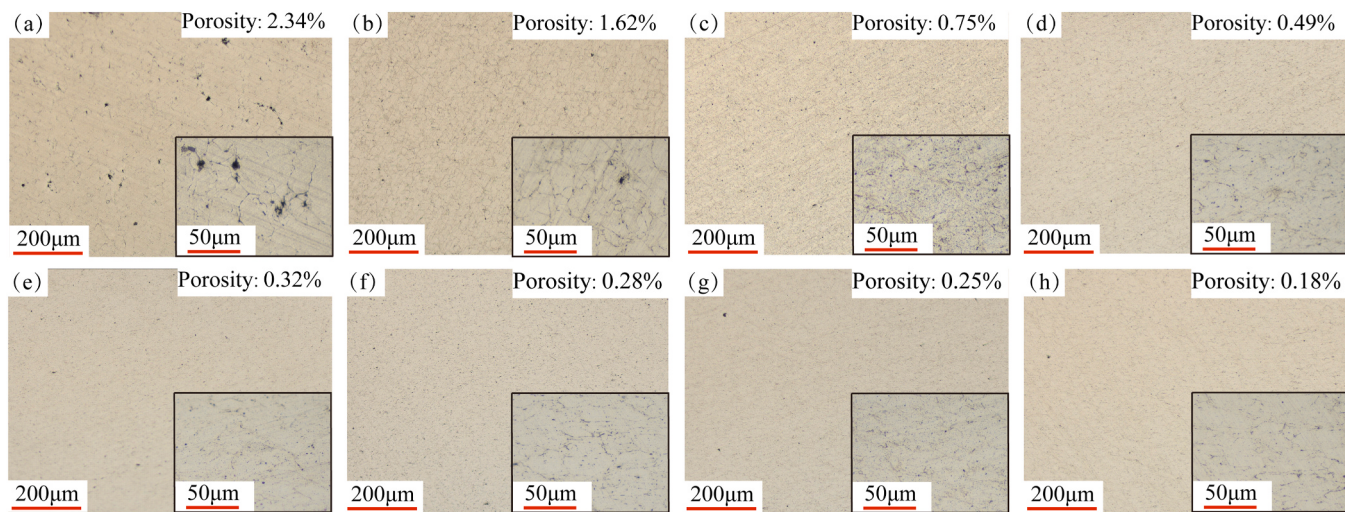


Fig. 3. Cross-sectional microstructures of CSAMed AA7050 materials: (a) As sprayed, (b) HT, (c) C-30, (d) C-50, (e) W, (f) A-6, (g) A-12, (h) A-24.

were reduced to 0.49%. Finally, Fig. 3(e-h) exhibits that the subsequent solid solution and aging treatments had a comparatively lesser effect on the material densification. The reason was that the majority of micro-defects in the AA7050 materials were repaired during annealing and hot compression. The microstructures of the samples after the solid solution and aging treatments were generally dense, with slightly reduced porosities.

The samples in different treatment states were observed after etching to further analyze the evolution of the samples microstructures, and the results are shown in Fig. 4. As can be seen in Fig. 4(a), due to the severe uneven deformation of the particles during the impact, the dynamic recrystallization occurred mainly in the impact area. Thus, the microstructure of as-sprayed samples tended to be inhomogeneous, exhibiting fine grains areas and coarse grains areas. The severe deformation of the particles also implied that significant work-hardening effects existed in the as-sprayed materials [34,35]. Moreover, micro-defects existed in the bonding sites of some of the multiple particles, as highlighted in the red dashed rectangular areas. Fig. 4(b) indicates that the high temperature during the annealing effectively promoted the homogenization of the microstructure of AA7050. On one hand, the boundaries among the particles were repaired under the effect of atomic diffusion, and the

particle boundaries became blurred. On the other hand, the recovery and recrystallization of the materials during the annealing alleviated the severe work-hardening effect, and equiaxial grains were prevalent in the samples. However, a few micro-pores that were ineffectively repaired could still be observed in the HT samples. Following subsequent hot compression, the microstructures of the AA7050 materials were basically free of visible micro-defects under the combined effect of high temperature and deformation, proving the necessity of introducing the thermo-mechanical coupling method to improve the microstructures of the CSAMed materials. The grains in the C-30 and C-50 samples were flattened, and the degree of flattening increased with increased compression. Finally, Fig. 4(e) shows that after solid solution treatment, the grains of the W samples evolve towards equiaxial shape with less flattening compared to the C-50 samples, attributed to the material recovery and recrystallization. Furthermore, given that the evolution of the grain morphologies mainly occurred in the solid solution stage, it was also observed that the OM images of the samples with different aging times did not substantially differ.

To investigate the effects of hot compression and solution-aging treatments on the microstructures of CSAMed AA7050 materials, the as-sprayed, C-50, and A-24 samples were selected for EBSD analysis.

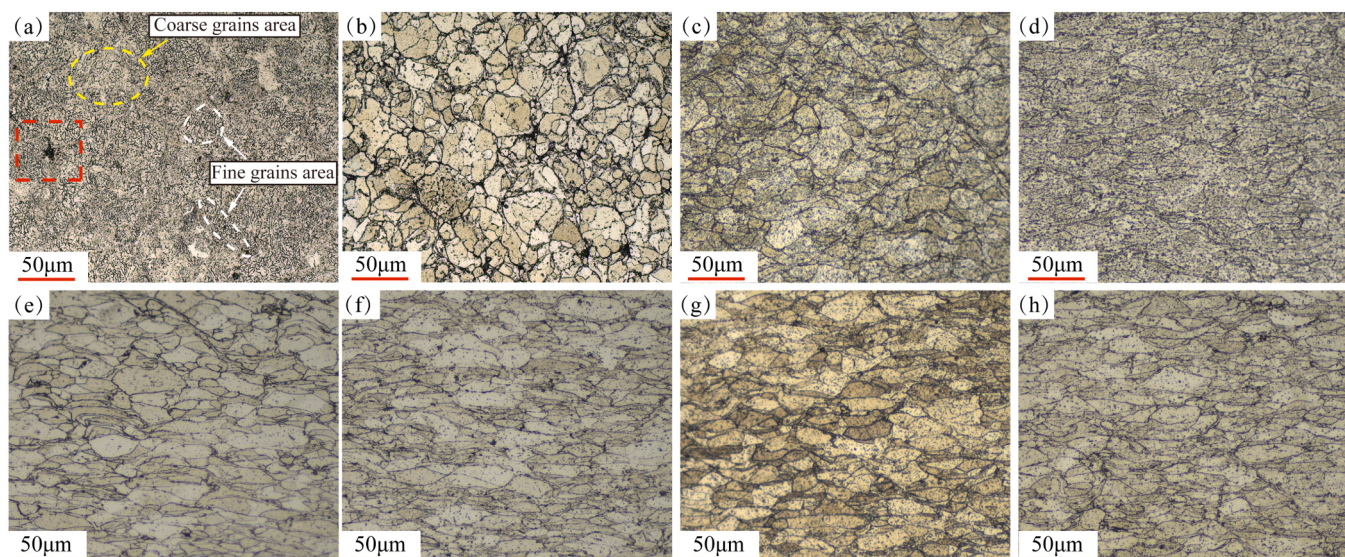


Fig. 4. Cross-sectional microstructures of CSAMed AA7050 materials after etching: (a) As sprayed, (b) HT, (c) C-30, (d) C-50, (e) W, (f) A-6, (g) A-12, (h) A-24.

Fig. 5 shows the inverse pole figures (IPFs) of the samples in different states, and the grains were distinguished by grain boundaries with misorientation $>15^\circ$. As observed **Fig. 5(a)**, the grains in the as-sprayed samples underwent significant deformation, with most grains exhibiting flattened shapes. In addition, by analyzing the distribution of coarse grains and fine grains, the fine grains were found to have a tendency of surrounding the coarse grains, as indicated by the black dashed elliptical areas. This phenomenon was attributed to the fact that dynamic recrystallization mainly occurred at the edge of the deformed particles during the impact, while the deformation inside the particles was relatively limited, resulting in less significant grains refinement [36]. Meanwhile, the unindexed areas of the samples were also mainly distributed at the edges of the particles, possibly due to the presence of micro-defects inside the samples or the formation of ultrafine grains smaller than the EBSD scanning step due to dynamic recrystallization [37]. Then, after annealing and hot compression treatments, flattened grains were prevalent in the C-50 samples. The unindexed areas were significantly reduced, which resulted from the growth of ultrafine grains due to annealing and hot compression and the repairing effect of post-treatments for micro-defects. In addition, the boundaries of the flattened grains of the C-50 samples exhibited a jagged shape, and fine equiaxed grains could be observed near part of the boundaries, implying that geometrically dynamic recrystallization might have occurred during the hot compression [38,39]. Finally, the grains of the A-24 samples were no longer significantly flattened after the solution-aging treatment, suggesting that the deformation energies due to compression were effectively released by the effects of recovery and recrystallization.

The grain boundaries were classified into high angle grain boundaries (HAGBs, $>15^\circ$) and low angle grain boundaries (LAGBs, $2^\circ\text{--}15^\circ$) to analyze the misorientation angle distributions of the AA7050 materials, and the results are shown in **Fig. 6**. As shown in **Fig. 6(a)**, severe deformation of the particles during the impact resulted in high-density subgrain structures, leading to a relatively high proportion of LAGBs in the as-sprayed samples. During the annealing and hot compression treatments, the high temperature and mechanical pressure provided sufficient energy to homogenize the microstructure of AA7050 materials. Thus, the proportion of LAGBs in the C-50 samples decreased. Then, the deformation energies from hot compression were released by the solid solution-aging treatment, further reducing the proportion of LAGBs in A-24 samples. According to Huang et al. [40], HAGBs could effectively hinder the dislocation movement, and a relatively high proportion of HAGBs could play a role in hardening and improving the mechanical properties of the materials.

Fig. 7 displays the IPFs of the samples at different stages of the treatment. First, the as-sprayed samples exhibited almost random texture. While after hot compression, the grains of the C-50 samples were aggregated towards $\langle 101 \rangle$ in the compression direction (Z) under external pressure, and the maximum intensity was slightly increased to 3.75, indicating that the grains were developing from random to very weak texture. Finally, when the C-50 samples were subjected to solid

solution-aging treatment, the grain orientation of the A-24 samples tended to be random again, and the maximum intensity decreased to 2.33. In general, no significant textures developed in the CSAMed AA7050 materials after the hybrid treatment.

The distributions of kernel averaged misorientation (KAM) of AA7050 materials in different states are shown in **Fig. 8**. By analyzing the KAM maps, it is possible to qualitatively analyze the degree and distribution of plastic deformation in different samples. As illustrated in **Fig. 8(a)**, the majority of the AA7050 particles underwent severe plastic deformation during the deposition, with deformation being more intense at the particle edges than within the particles. Then, the overall severe localized deformation of AA7050 materials was effectively mitigated, after annealing and hot compression treatment. Finally, the solution-aging treatment effectively released the deformation energies of the C-50 samples, and the localized deformation in most areas of the A-24 samples was further relieved with a more homogeneous distribution.

Fig. 9 presents the SEM images (in BSE mode) of secondary phases in different states and the TEM image of the A-6 samples. As shown in **Fig. 9(a)**, there was dendritic solute segregation in the as-sprayed samples. The EDS point analysis of P1 revealed that the elemental composition (in at%) of the solute segregation area was 89.32% Al, 5.11% Mg, 3.61 Zn, and 1.95% Cu. This dendritic microstructure was caused by the high rate of cooling of the powder during atomized production [25], which was retained in the as-sprayed material due to the low temperature of the cold spraying process. Then, it can also be seen in **Fig. 9** that there were relatively significant differences in the morphology and size of the secondary phases in the different state samples. For AA7xxx series alloys, secondary phases such as AlMgZnCu, Al₂CuMg, and Al₇Cu₂Fe may form during heat treatment [41]. The elemental composition of the marked points in **Fig. 9** was analyzed using EDS, and the results are presented in **Table 4**. Combining the EDS results with the SEM images revealed that after the annealing treatment, the dendritic microstructures were no longer present in the HT samples due to the re-dissolution of solutes. The secondary phases appearing in the deposits were dominated by AlMgZnCu. While, after hot compression, the volume of the secondary phases in the C-50 samples increased and Al₂CuMg appeared. Meanwhile, solid solution and aging treatments played significant roles in the evolution of the secondary phases, and it could be seen that AlMgZnCu and Al₂CuMg were found in both A-6 and A-24 samples. However, due to the longer holding time, the density of the secondary phases in the A-24 sample was significantly reduced and increased in size compared to aging for 6 hours. Moreover, as shown by the position of the yellow arrow in **Fig. 9(e)**, rod-like secondary phases were present in A-24 samples. The EDS analysis results showed that the elemental composition (in at%) of this secondary phase was 86.16% Al, 7.11% Cu, 2.80% Fe, 2.75% Mg and 1.19% Zn. Therefore, it could be inferred that after 24 hours of aging, relatively large-sized Al₇Cu₂Fe phases appeared in the deposits, which might deteriorate the ductility of the materials [30,42]. **Fig. 9(f)** shows the TEM bright field image of the intragranular

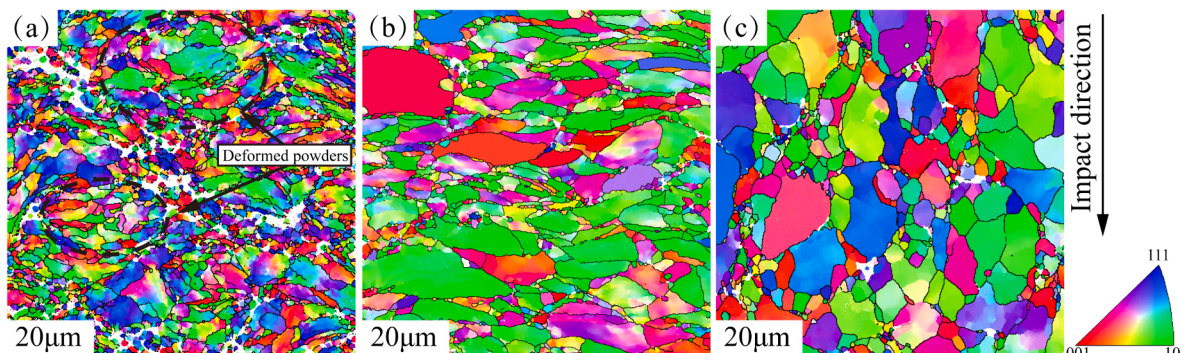


Fig. 5. EBSD images of the CSAMed AA7050 materials: (a) As sprayed, (b) C-50, (c) A-24.

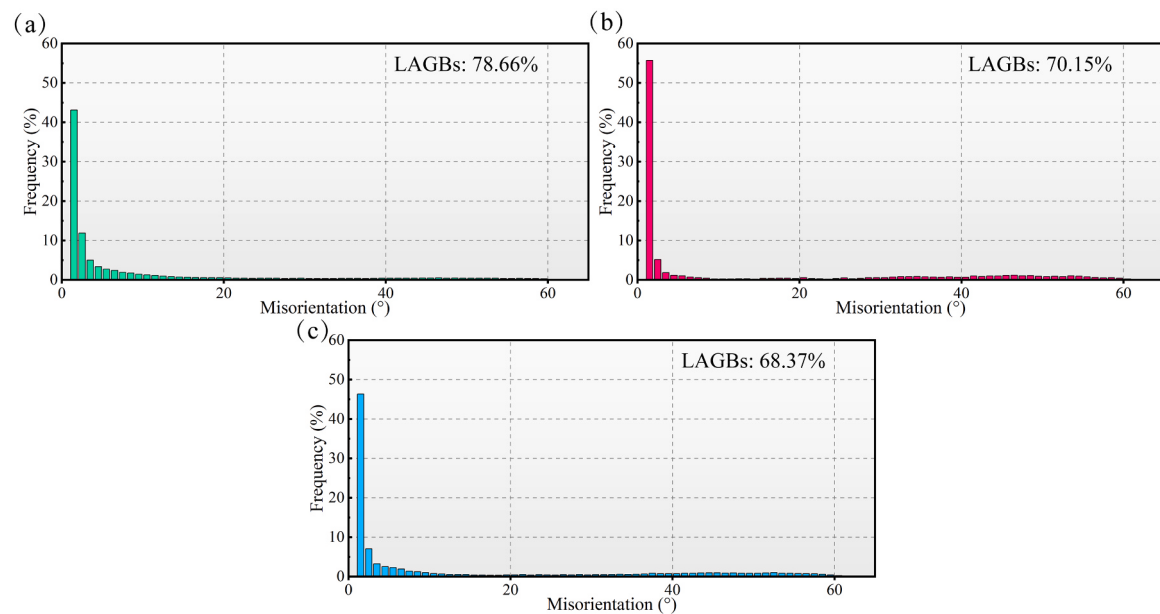


Fig. 6. Misorientation angle distributions of the CSAMed AA7050 materials: (a) As sprayed, (b) C-50, (c) A-24.

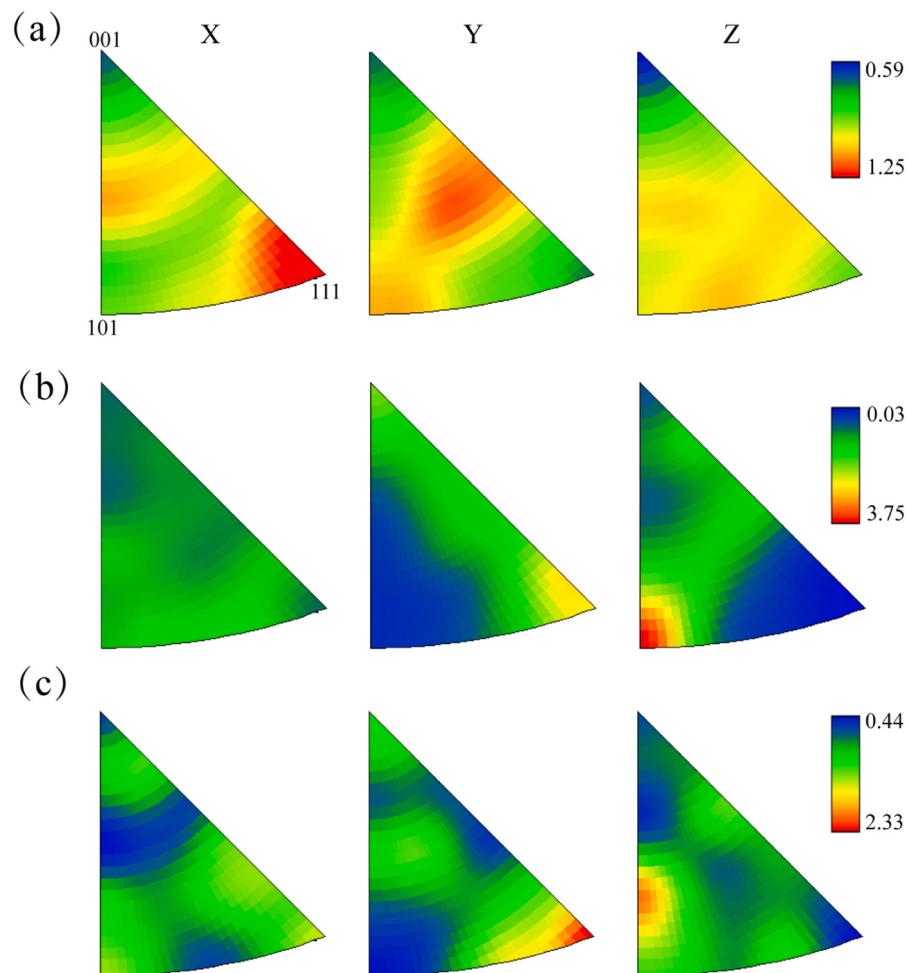


Fig. 7. IPFs of the CSAMed AA7050 materials: (a) As sprayed, (b) C-50, (c) A-24.

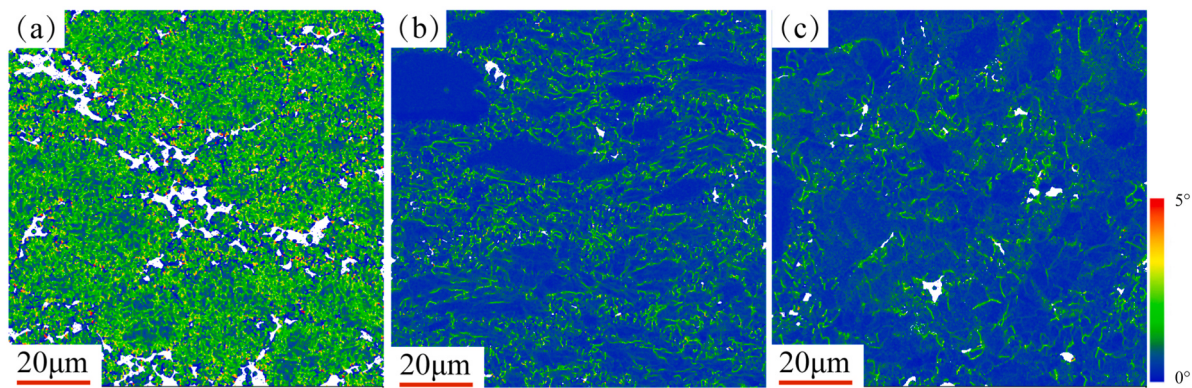


Fig. 8. KAM maps of the CSAMed AA7050: (a) As sprayed, (b) C-50, (c) A-24.

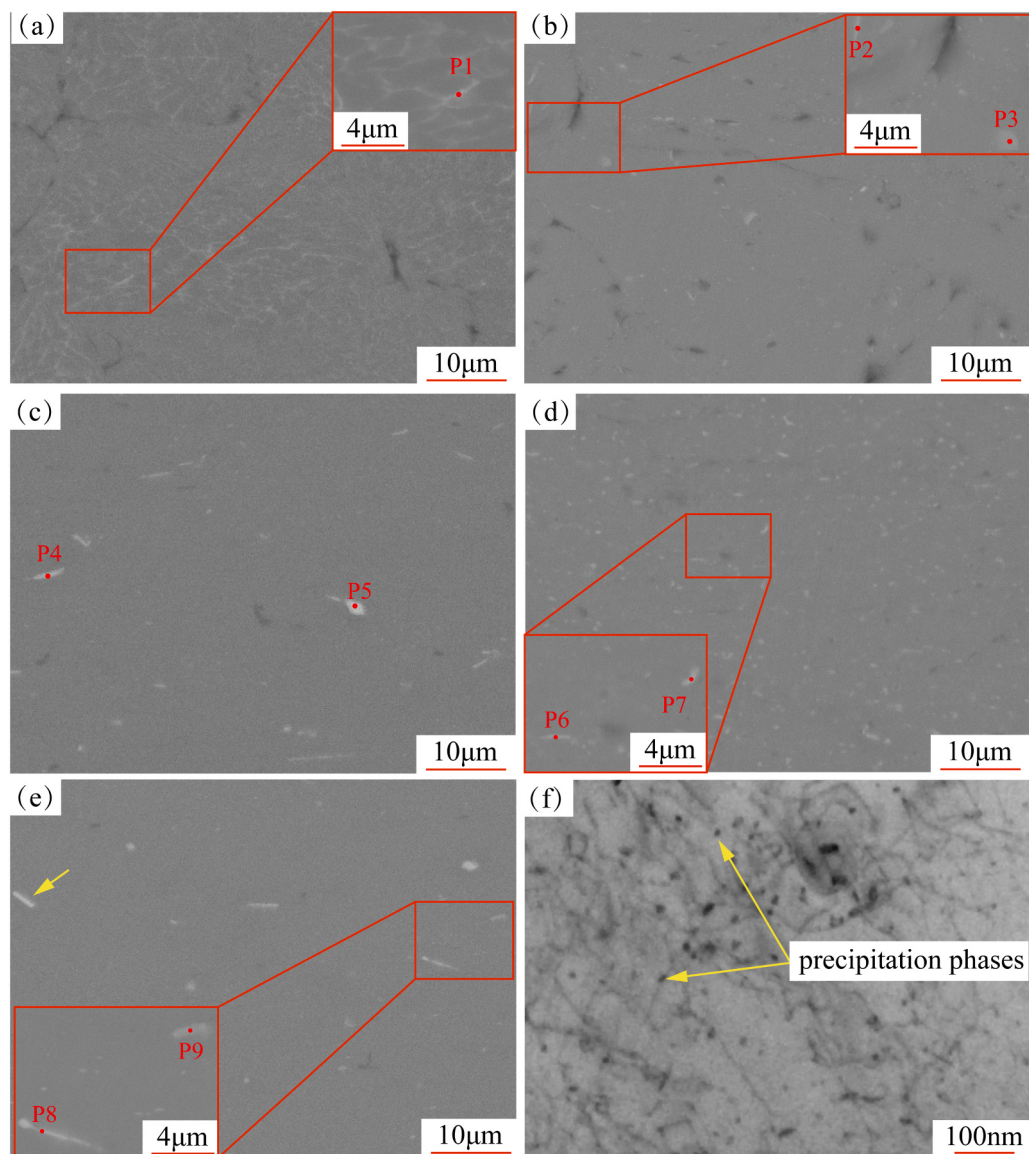


Fig. 9. SEM (a-e) and TEM images (f) of CSAMed AA7050 samples: (a) As sprayed, (b) HT, (c) C-50, (d) A-6, (e) A-24, (f) bright field image of A-6 sample.

Table 4
EDS point analysis results of samples in different states (at%).

	Al	Mg	Zn	Cu	Possible phase
P2	94.32	2.02	1.99	1.67	AlMgZnCu
P3	93.54	2.58	1.81	2.07	AlMgZnCu
P4	85.57	5.59	1.09	7.75	Al ₂ CuMg
P5	90.32	3.60	1.47	4.61	Al ₂ CuMg
P6	89.01	5.87	1.67	3.45	Al ₂ CuMg
P7	94.01	2.13	1.99	1.87	AlMgZnCu
P8	92.87	2.99	1.90	2.25	AlMgZnCu
P9	92.07	2.78	1.57	3.58	Al ₂ CuMg

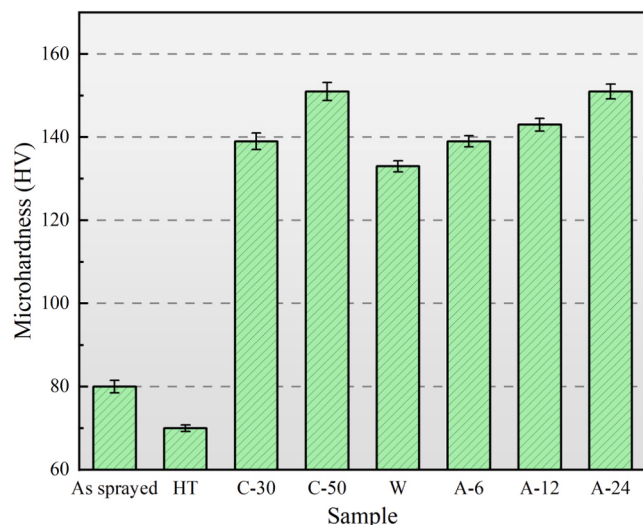


Fig. 10. Microhardness of CSAMed AA7050 materials in different states.

precipitation phases of the A-6 samples. For AA7xxx materials, the main strengthening phase η' phase is usually preferentially precipitated [43]. Therefore, after the 6 hours aging treatment, the A-6 samples precipitated a certain amount of fine η' phases, which could effectively provide a strengthening effect on the materials.

3.2. Mechanical Properties

3.2.1. Microhardness

Fig. 10 presents the variation of microhardness of AA7050 materials in different states. In general, the nature of material strengthening is to impede dislocation movement [25]. The evolution of strengthening mechanisms leads to changes in the mechanical properties of materials. Firstly, the as-sprayed AA7050 materials exhibit a microhardness of about 80 HV, attributable to work-hardening and fine grain structures caused by high-speed impact. Then, for the annealed and hot compressed samples, as the recovery effect played a dominant role in the microhardness evolution of the materials, the microhardness of the HT samples decreased to approximately 75 HV after annealing. While microhardness of AA7050 increased significantly after hot compression, and the increase was more obvious with the increase of compression. The microhardness of the C-30 and C-50 samples reached approximately 139 and 151 HV, respectively. This increase was attributed to the dynamic recrystallization of the AA7050 material during hot deformation, which produced a fine grain structure, as well as the work hardening caused by the deformation. In addition, as a highly alloyed alloy, aluminum alloys tend to precipitated with multiple phases in the matrix during thermal deformation [44]. These precipitated phases can significantly increase the microhardness of aluminum alloys. Finally, for aged samples, the duration of aging treatment had a pronounced effect on the microhardness. After the solid solution treatment, the

microhardness initially decreased and then slowly increased with the aging time. The precipitation sequence of the 7-series aluminum alloys during artificial aging treatment is supersaturated solid solution (SSS) \rightarrow Guinier-Preston (GP) zones \rightarrow metastable η' phase \rightarrow equilibrium η phase, and the transition of the main strengthening phase η' phase to the η phase usually occurs above 180 °C or after long period of time at low aging temperatures [45,46]. The microhardness variation in aged samples originated from the competition among different strengthening mechanisms. Following solution treatment, the microhardness of W samples decreased due to the recovery effect of the high temperature that effectively alleviated the work hardening of the hot compression samples. During the subsequent artificial aging process, the internal stresses within the materials could be further reduced with increased aging time. However, the strengthening mechanism that played a dominant role in this stage changed to precipitation strengthening, where the volume fraction and distribution homogeneity of the η' phase increased with time, contributing to the increase in microhardness.

3.2.2. Tensile properties

The mechanical properties of CSAMed AA7050 materials in different states are presented in Fig. 11. The mechanical properties of CSAMed materials depend on the conventional strengthening mechanism and the inter-particle bonding states [47]. Due to the remarkable improvement in the mechanical properties after treatment, the stress-strain curves of the samples in the sprayed state are not drawn in Fig. 11(a) and instead replaced by star symbols to more clearly show the ultimate tensile strength (UTS) and elongation at fracture (EL) of the as-sprayed materials. Fig. 11(b) summarizes the evolution of the mechanical properties of the CSAMed AA7050 materials in different states. First, as a result of the "plasticity depletion" effect during cold spraying and the poor inter-particle bonding, the as-sprayed AA7050 materials showed almost no plastic deformability and only 127.5 MPa of strength. After the annealing treatment, the strength of the HT samples increased to 223.7 MPa, which was mainly attributed to the repair of the inter-particle interfaces during the annealing process, whereas the improvement in ductility was attributed to the recovery and recrystallization relieved the work hardening of the as-sprayed materials. The hot compression treatment then further improved the mechanical properties of the AA7050 materials. The UTS and EL of C-30 and C-50 samples increased to 253.4 MPa, 5.5% and 319.8 MPa, 7.8%, respectively, with the increase of reduction. The improvements in the mechanical properties of the materials through hot compression were mainly due to the repair of micro-defects of the materials by the external pressure. Meanwhile, the increased reduction led to a more significant dynamic recrystallization, resulting in the formation of more recrystallized structures, which could also effectively improve the strength and ductility of the materials. From the above results, combined with the microstructure analysis, it could be seen that for the annealed and hot compressed samples, although there were differences in their mechanical properties, the repair of micro-defects such as the inter-particle bonding was the main reason for the enhancement of the mechanical properties in this stage. The role of other strengthening mechanisms was relatively insignificant. As a result, the tensile strength and ductility of the C-50 samples were improved compared with the HT and C-30 samples since the majority of the defects in the samples were effectively repaired after 50% compression.

However, during the subsequent solution-aging treatment, while the strength of the CSAMed AA7050 materials continuously increased with the aging time, the ductility initially increased and then decreased. When the artificial aging time was increased from 0 to 24 hours, the UTS of the samples increased from 397.7 MPa to 557.7 MPa, which was 337.4% higher compared to the as-sprayed samples. The EL of AA7050 materials reached the peak value of 20.5% at 6 hours of aging, which increased by 1173.2% compared with the as-sprayed samples. With further prolongation of the aging time, the EL began to decrease, and the EL of the A-24 sample was about 11.3%. The evolution of the

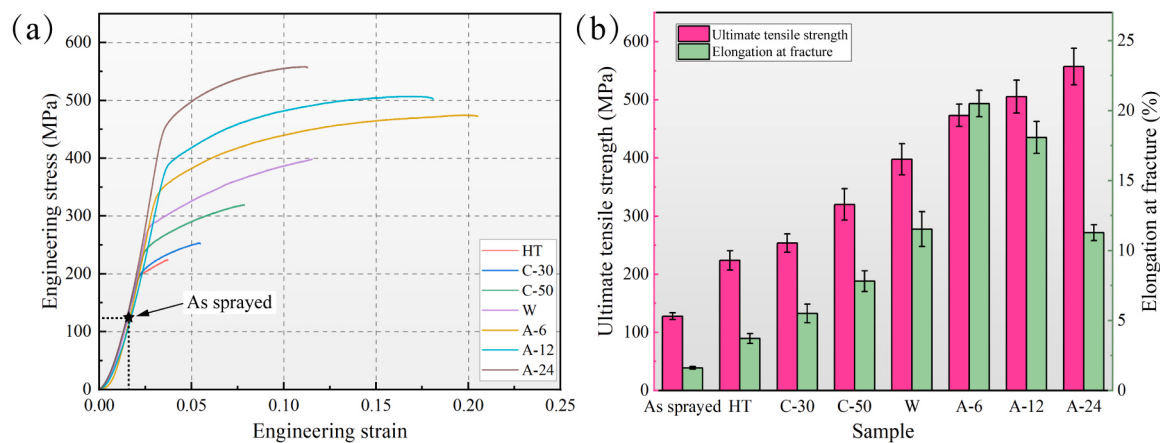


Fig. 11. Tensile strength of the CSAMed AA7050 materials: (a) stress-strain curves, (b) UTS and EL.

strengthening mechanism was responsible for the above-mentioned changes in the mechanical properties of the CSAMed AA7050 materials during the aging process. The solid solution treatment could further improve the microstructure of the materials while alleviating the work hardening caused by hot compression, so the mechanical properties of the W samples were further improved compared to the C-50 samples. In the subsequent aging process, the microstructure of the material could be further repaired. Nevertheless, considering that the internal micro-defects of the materials were almost repaired at this stage, the effects of microstructure repair on the mechanical properties of the materials were reduced. At this stage, precipitation strengthening played a dominant role in the evolution of the mechanical properties of the CSAMed AA7050 and became more pronounced with time. However, when the aging time was too long, a small part of the η' phases transformed into η phases [48–51]. Meanwhile, the results of microstructure analysis also indicated that extended aging time resulted in the appearance of coarse secondary phases in the materials. These η phases and secondary phases could further increased the strength of the bulk materials by hindering the dislocation movement, but at the same time led to strain localization, which decreased the EL of the CSAMed AA7050 materials.

To further analyze the evolution of the strengthening mechanism of the material during the post-treatment, radar charts were used to qualitatively discuss the strengthening mechanism of AA7050 at different stages by combining the microstructure analysis results, as shown in Fig. 12. Since as-sprayed AA7050 did not generate effective strengthening phases and the impact deformation resulted in high dislocation density and fine grains, solid solution strengthening, work hardening and grain refinement are its main strengthening mechanisms. However, the weak interparticle bonding severely limited the ductility of materials. After annealing and hot compression treatment, the grain size of the C-50 sample grew, the work hardening was significantly alleviated, and the initial solid solution strengthening developed towards precipitation strengthening. Meanwhile, the bonding state of the particle boundaries improved significantly. Therefore, the main strengthening mechanisms of C-50 samples are relatively good interparticle bonding state, precipitation and work hardening. Compared with the C-50 sample, the A-24 sample exhibited much more precipitation strengthening, less work hardening, and a denser microstructure without any significant change in grain size. Therefore, for aging samples, the main strengthening mechanism is a combination of improved interparticle bonding and precipitation strengthening.

Fig. 13 exhibits the fracture surfaces of AA7050 specimens in different treatment states. In Fig. 13(a), the as-sprayed samples exhibited typical brittle fracture observed in CSAMed materials. Dimples were absent in the fracture surfaces, and the interface between particles was clearly visible. Moreover, areas of significantly poor inter-particle bonding could be identified, as shown in the red dashed rectangle area. In the HT samples, the bonding interface between the particles became blurred, and some of the well-bonded areas developed dimples during tensile tests (as indicated by the red arrows). However, there were also poorly bonded areas as indicated by the yellow arrows. Therefore, the fracture of HT samples showed mixed mode and was dominated by brittle fracture. The analysis results in Fig. 13(c) and (d) showed that after compression, obvious tear ridges and dimples existed within the fracture of C-30 and C-50. Compared to the C-30 sample, the C-50 dimples occupied larger areas, indicating superior ductility while also suggesting that the C-50 sample had a better particle bonding state. However, there were still a few micro-defects found inside the C-50 fracture surfaces as shown by the red arrows. These defects limited the strength of the bulk materials by acting as areas of stress concentration during the tensile tests. In the fracture surfaces of W and A-6 specimens shows in Fig. 13(e) and (f), tear ridges with more dimples could be observed. Especially for the A-6 sample, the large dimples were almost spread over the fracture surfaces, and no obvious micro-defect was found. This indicated that the solution-aging treatment effectively restored the ductility of the materials and further improved the interparticle interface bonding. Compared with sample A-6, the number of

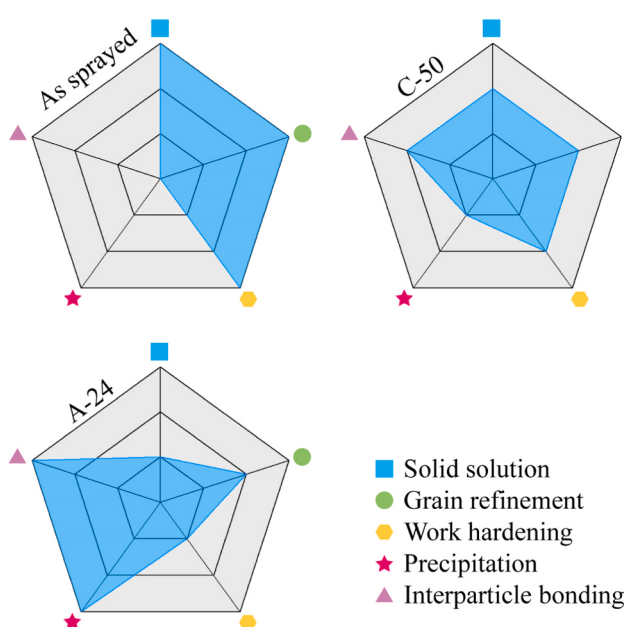


Fig. 12. Radar charts of strengthening mechanisms in different states AA7050 deposits.

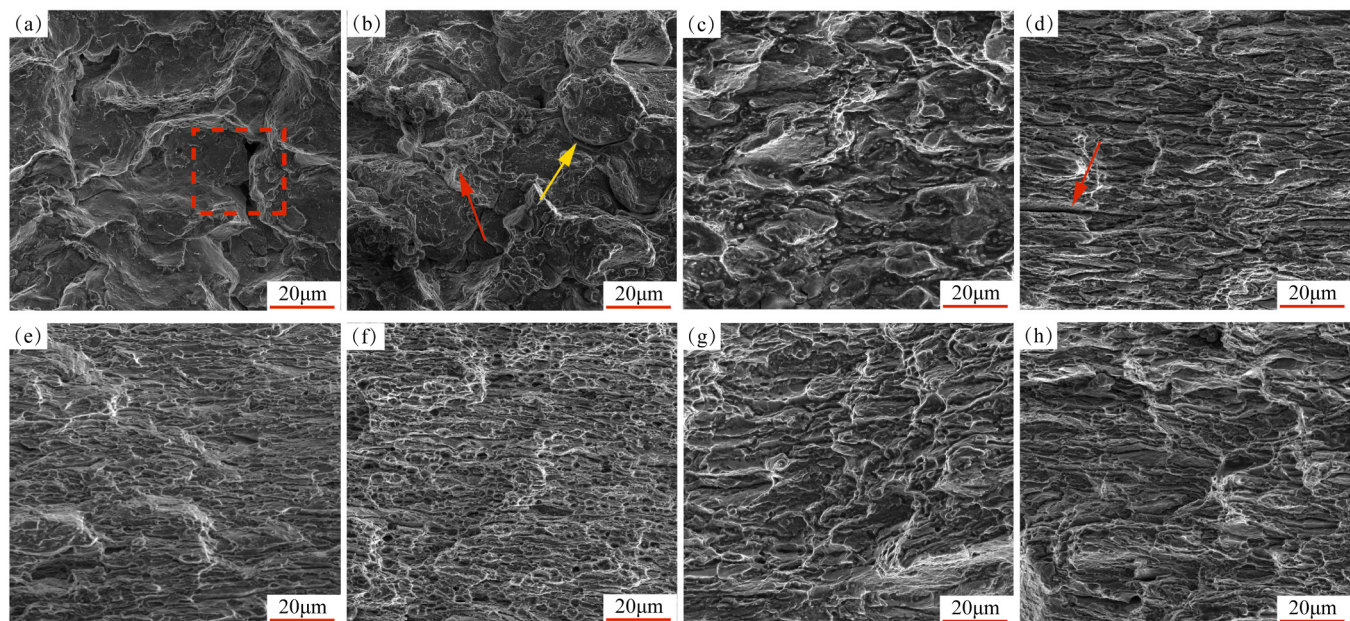


Fig. 13. Fracture surfaces of CSAMed AA7050 materials: (a) As sprayed, (b) HT, (c) C-30, (d) C-50, (e) A-0, (f) A-6, (g) A-12, (h) A-24.

dimples at the fracture surfaces of samples A-12 and A-24 decreased, suggesting that the ductility of the materials showed a decreasing trend, which was consistent with the tensile test results.

4. Conclusions

In this study, a hybrid post-treatment method of CSAMed deposits (i.e., annealing + hot compression + solid solution-aging treatment) was proposed. The results indicated that the hybrid post-treatment could effectively improve the microstructure and enhance the mechanical properties of CSAMed AA7050 materials. The main conclusions of this work are as follows:

- (1) The hybrid post-treatment could effectively improve the densification of CSAMed AA7050 materials, with hot compression having the most significant effect on the repair of micro-defects and the healing of inter-particle bond interfaces. The porosities of the samples were reduced from 2.34% to 0.18% after hybrid post-treatment.
- (2) The microstructure homogeneity of CSAMed AA7050 materials was significantly improved after the hybrid post-treatment. After 24 hours of aging treatment, the grains of the materials no longer appeared obviously flattened, and the severe work-hardening and uneven deformation distribution were also effectively alleviated.
- (3) Only HT samples with lower microhardness than the as-sprayed samples, whereas the hot compression significantly increased the microhardness of the materials. Furthermore, the microhardness of the CSAMed AA7050 materials reached about 150 HV after solid solution and aging treatment.
- (4) The hybrid post-treatment significantly improved the tensile properties of the AA7050 materials. During the hybrid post-treatment, the ultimate tensile strength of the CSAMed AA7050 bulk materials gradually increased. The strength of the samples after aging for 24 hours reached 557.7 MPa, which was 337.4% higher compared to the as-sprayed samples. Meanwhile, the samples after aging for 6 hours exhibited the best plastic deformability, and the elongation at fracture reached 20.5%, an increase of 1173.2% compared with the as-sprayed samples. The fracture surfaces of the specimens also indicated that the ductility of the materials was effectively restored during the hybridization

post-treatment, and the fracture mechanism gradually changed from brittle fracture to ductile fracture.

CRediT authorship contribution statement

Chengxin Liu: Investigation, Conceptualization, Methodology, Formal analysis, Writing - original draft. **Xingrong Chu:** Conceptualization, Project administration, Formal analysis, Funding acquisition, Writing - original draft. **Naijiang Wang:** Investigation, Data curation, Validation. **Jun Gao:** Supervision, Resources, Writing - review & editing. **Liang Chen:** Supervision, Writing - review & editing.

Declaration of Competing Interest

The authors declare that they have no known competing financial interests or personal relationships that could have appeared to influence the work reported in this paper.

Data Availability

Data will be made available on request.

Acknowledgment

The authors would like to acknowledge the financial support from National Natural Science Foundation of China (Grant No. 52175339, 52222510) and Key Research and Development Program of Shandong Province (Grant No. 2021CXGC010304).

References

- [1] A. Navabi, M. Vandadi, T. Bond, V. Rahneshin, J. Obayemi, R. Ahmed, J. E. Ogheneweta, V. Champagne, N. Rahbar, W.O. Soboyejo, Deformation and cracking phenomena in cold sprayed 6061 Al alloy powders with nanoscale aluminum oxide films, Mater. Sci. Eng. A. 841 (2022) 143036, <https://doi.org/10.1016/j.msea.2022.143036>.
- [2] M. Amiri, G.A. Crawford, J.C. Earthman, Quantitative percussion diagnostics for evaluating porosity and surface roughness of cold sprayed and laser deposited materials, J. Mater. Res. Technol. 14 (2021) 312–323, <https://doi.org/10.1016/j.jmrt.2021.06.047>.
- [3] W. Li, C. Cao, S. Yin, Solid-state cold spraying of Ti and its alloys: a literature review, Prog. Mater. Sci. 110 (2020) 100633, <https://doi.org/10.1016/j.pmatsci.2019.100633>.

- [4] X. Fan, X. Chu, Y. Xie, D. Zhou, Q. Tian, Y. Tong, P.K. Liaw, S. Chen, F. Meng, Microstructure and mechanical properties of cold spray additive manufactured and post heat treated high-entropy alloys with mixed CoCrFeNi and Ti powders, *J. Mater. Res. Technol.* 27 (2023) 4328–4344, <https://doi.org/10.1016/j.jmrt.2023.10.274>.
- [5] C.S. Witharamage, M.A. Alrizqi, J. Chirstudasjustus, A.A. Darwish, T. Ansell, A. Nieto, R.K. Gupta, Corrosion-resistant metallic coatings for aluminum alloys by cold spray, *Corros. Sci.* 209 (2022) 110720, <https://doi.org/10.1016/j.corsci.2022.110720>.
- [6] X. Zhang, S. Wu, W. Liu, X. Chu, Y. Xie, F. Zhang, High performance tin-based Babbitt coatings deposited by high-pressure cold spraying, *Surf. Coat. Technol.* 473 (2023) 130048, <https://doi.org/10.1016/j.surfcoat.2023.130048>.
- [7] S. Kumar, A.S. Dhavale, N.M. Chavan, S. Acharya, Superconducting niobium coating deposited using cold spray, *Mater. Lett.* 312 (2022) 131715, <https://doi.org/10.1016/j.matlet.2022.131715>.
- [8] Z. Mohammadzaki Goudarzi, Z. Valefi, P. Zamani, S. Taghi-Ramezani, Comparative investigation of the effect of composition and porosity gradient on thermo-mechanical properties of functionally graded thick thermal barrier coatings deposited by atmospheric plasma spraying, *Ceram. Int.* 48 (2022) 28800–28814, <https://doi.org/10.1016/j.ceramint.2021.12.307>.
- [9] X. Xie, S. Yin, R. nirina Raolison, C. Chen, C. Verdy, W. Li, G. Ji, Z. Ren, H. Liao, Al matrix composites fabricated by solid-state cold spray deposition: a critical review, *J. Mater. Sci. Technol.* 86 (2021) 20–55, <https://doi.org/10.1016/j.jmst.2021.01.026>.
- [10] C.M. Sample, V.K. Champagne, A.T. Nardi, D.A. Lados, Factors governing static properties and fatigue, fatigue crack growth, and fracture mechanisms in cold spray alloys and coatings/repairs: a review, *Addit. Manuf.* 36 (2020) 101371, <https://doi.org/10.1016/j.addma.2020.101371>.
- [11] A. Günen, Ü. Gürol, M. Koçak, G. Çam, A new approach to improve some properties of wire arc additively manufactured stainless steel components: simultaneous homogenization and bonding, *Surf. Coat. Technol.* 460 (2023), <https://doi.org/10.1016/j.surfcoat.2023.129395>.
- [12] R. Shanhar, K. Chen, C. Abeykoon, Powder-based additive manufacturing: a critical review of materials, methods, opportunities, and challenges, *Adv. Eng. Mater.* 25 (2023), <https://doi.org/10.1002/adem.202300375>.
- [13] G. Çam, Prospects of producing aluminum parts by wire arc additive manufacturing (WAAM), *Mater. Today Proc.* 62 (2022) 77–85, <https://doi.org/10.1016/j.mtpr.2022.02.137>.
- [14] S. Yin, N. Fan, C. Huang, Y. Xie, C. Zhang, R. Lupoi, W. Li, Towards high-strength cold spray additive manufactured metals: Methods, mechanisms, and properties, *J. Mater. Sci. Technol.* 170 (2024) 47–64, <https://doi.org/10.1016/j.jmst.2023.05.047>.
- [15] G. Prashar, H. Vasudev, A comprehensive review on sustainable cold spray additive manufacturing: State of the art, challenges and future challenges, *J. Clean. Prod.* 310 (2021) 127606, <https://doi.org/10.1016/j.jclepro.2021.127606>.
- [16] C. Huang, M. Arseenko, L. Zhao, Y. Xie, A. Eelsenberg, W. Li, F. Gärtner, A. Simar, T. Klassen, Property prediction and crack growth behavior in cold sprayed Cu deposits, *Mater. Des.* 206 (2021) 109826, <https://doi.org/10.1016/j.mtodes.2021.109826>.
- [17] K. Wu, A. Aprilia, S.C. Tan, W. Zhou, Rapid post processing of cold sprayed Inconel 625 by induction heating, *Mater. Sci. Eng. A.* 872 (2023) 144955, <https://doi.org/10.1016/j.msea.2023.144955>.
- [18] N. Fan, A. Rafferty, R. Lupoi, W. Li, Y. Xie, S. Yin, Microstructure evolution and mechanical behavior of additively manufactured CoCrFeNi high-entropy alloy fabricated via cold spraying and post-annealing, *Mater. Sci. Eng. A.* 873 (2023) 144748, <https://doi.org/10.1016/j.msea.2023.144748>.
- [19] A. Bhowmik, A. Wei-Yee Tan, W. Sun, Z. Wei, I. Marinescu, E. Liu, On the heat-treatment induced evolution of residual stress and remarkable enhancement of adhesion strength of cold sprayed Ti-6Al-4V coatings, *Results Mater.* 7 (2020) 100119, <https://doi.org/10.1016/j.rimma.2020.100119>.
- [20] D. Shrestha, F. Azarmi, X.W. Tangpong, Effect of Heat Treatment on Residual Stress of Cold Sprayed Nickel-based Superalloys, *J. Therm. Spray. Technol.* 31 (2022) 197–205, <https://doi.org/10.1007/s11666-021-01284-x>.
- [21] Y. Ren, N. ul Haq Tariq, H. Liu, X. Cui, Y. Shen, J. Wang, T. Xiong, Remarkable improvement in microstructure and mechanical properties of cold sprayed Al deposits via impact forging post-spray treatment, *Mater. Today Commun.* 32 (2022) 103951, <https://doi.org/10.1016/j.jmtcomm.2022.103951>.
- [22] X. Ye, M. Yu, Q. Huang, J. Qin, H. Li, M.P. Planche, H. Liao, X. Suo, Evolution of microstructures and mechanical properties of cold sprayed copper in hot rolling, *J. Therm. Spray. Technol.* 32 (2023) 2701–2712, <https://doi.org/10.1007/s11666-023-01655-6>.
- [23] Y.K. Wei, X.T. Luo, X. Chu, G.S. Huang, C.J. Li, Solid-state additive manufacturing high performance aluminum alloy 6061 enabled by an in-situ micro-forging assisted cold spray, *Mater. Sci. Eng. A.* 776 (2020) 139024, <https://doi.org/10.1016/j.msea.2020.139024>.
- [24] D. Wu, W. Li, K. Liu, Y. Yang, S. Hao, Optimization of cold spray additive manufactured AA2024/Al2O3 metal matrix composite with heat treatment, *J. Mater. Sci. Technol.* 106 (2022) 211–224, <https://doi.org/10.1016/j.jmst.2021.07.036>.
- [25] Y. Ren, D. Zhou, G. Xie, H. Liu, X. Cui, J. Wang, T. Xiong, Effects of different heat treatments on anisotropy of cold sprayed 7075 Al deposits, *Mater. Charact.* 199 (2023) 112828, <https://doi.org/10.1016/j.matchar.2023.112828>.
- [26] J. Zuo, L. Hou, X. Shu, W. Peng, A. Yin, J. Zhang, Effect of deformation on precipitation and the microstructure evolution during multistep thermomechanical processing of Al-Zn-Mg-Cu alloy, *Metals* 10 (2020) 1–16, <https://doi.org/10.3390/met10111409>.
- [27] M. Erol, A. Kısasöz, P. Yaman, S.S. Karabeyoğlu, U. Barut, A study on high temperature dry sliding wear of AA7050-T4 and effects of the test temperature on microstructure, corrosion behavior, hardness and electrical conductivity, *Mater. Today Commun.* 31 (2022), <https://doi.org/10.1016/j.jmtcomm.2022.103410>.
- [28] L. Jiang, Z. Zhang, H. Fu, S. Huang, D. Zhuang, J. Xie, Corrosion behavior and mechanism of Al-Zn-Mg-Cu alloy based on the characterization of the secondary phases, *Mater. Charact.* 189 (2022) 111974, <https://doi.org/10.1016/j.matchar.2022.111974>.
- [29] T. Liu, H. Jiang, H. Sun, Y. Wang, Q. Dong, J. Zeng, F. Bian, J. Zhang, F. Chen, B. Sun, Effects of rolling deformation on precipitation behavior and mechanical properties of Al-Zn-Mg-Cu alloy, *Mater. Sci. Eng. A.* 847 (2022) 143342, <https://doi.org/10.1016/j.mseaa.2022.143342>.
- [30] S. Yang, Z. Li, Y. Zhou, Z. Tan, C. Kong, H. Yu, Edge-crack free and high mechanical properties of AA7075 sheets by using cryorolling and subsequent aging, *J. Alloy. Compd.* 931 (2023) 167556, <https://doi.org/10.1016/j.jallcom.2022.167556>.
- [31] M.M.Z. Ahmed, M.M. El-Sayed El-Sayed, D. Fydrych, G. Çam, Friction Stir Welding of Aluminum in the Aerospace Industry: The Current Progress and State-of-the-Art Review, *Materials* 16 (2023), <https://doi.org/10.3390/ma16082971>.
- [32] B. Anandan, M. Manikandan, Effect of welding speeds on the metallurgical and mechanical property characterization of friction stir welding between dissimilar aerospace grade 7050 T7651-2014A T6 aluminum alloys, *Mater. Today Commun.* 35 (2023) 106246, <https://doi.org/10.1016/j.jmtcomm.2023.106246>.
- [33] D. Yuan, L. Tan, K. Chen, S. Chen, P. Xie, H. Jiao, Comparison of strength, stress corrosion cracking and microstructure of new generation 7000 series aluminium alloys, *Mater. Sci. Technol. (U. Kingd.)*, 37 (2021) 616–623, <https://doi.org/10.1080/02670836.2021.1938838>.
- [34] J. Tam, B. Yu, W. Li, D. Poirier, J.G. Legoux, J.D. Giallonardo, J. Howe, U. Erb, The effect of annealing on trapped copper oxides in particle-particle interfaces of cold-sprayed Cu coatings, *Scr. Mater.* 208 (2022) 114333, <https://doi.org/10.1016/j.scriptamat.2021.114333>.
- [35] L. Yang, P. Wang, X. Luo, H. Li, H. Yang, S. Wang, Q. Li, Nanocrystallization of interfacial microstructure of deformed particles in cold sprayed Ti6Al4V deposits, *Mater. Des.* 210 (2021) 110117, <https://doi.org/10.1016/j.matedes.2021.110117>.
- [36] C. Chen, Y. Xie, S. Yin, W. Li, X. Luo, X. Xie, R. Zhao, C. Deng, J. Wang, H. Liao, M. Liu, Z. Ren, Ductile and high strength Cu fabricated by solid-state cold spray additive manufacturing, *J. Mater. Sci. Technol.* 134 (2023) 234–243, <https://doi.org/10.1016/j.jmst.2022.07.003>.
- [37] J.Y. Lek, A. Bhowmik, A.W.Y. Tan, W. Sun, X. Song, W. Zhai, P.J. Buenconsejo, F. Li, E. Liu, Y.M. Lam, C.B. Boothroyd, Understanding the microstructural evolution of cold sprayed Ti-6Al-4V coatings on Ti-6Al-4V substrates, *Appl. Surf. Sci.* 459 (2018) 492–504, <https://doi.org/10.1016/j.apsusc.2018.07.175>.
- [38] N. ul H. Tariq, L. Gyansah, X. Qiu, C. Jia, H. Bin Awais, C. Zheng, H. Du, J. Wang, T. Xiong, Achieving strength-ductility synergy in cold spray additively manufactured Al/B 4C composites through a hybrid post-deposition treatment, *J. Mater. Sci. Technol.* 35 (2019) 1053–1063, <https://doi.org/10.1016/j.jmst.2018.12.022>.
- [39] N. Raja, A. Kumar, S.K. Patel, Hot deformation and microstructural evolution of ultrasonically fabricated as-cast Al-7.3Zn-2.2Mg-2Cu alloy, *Mater. Charact.* 206 (2023) 113404, <https://doi.org/10.1016/j.matchar.2023.113404>.
- [40] C. Huang, W. Li, Y. Feng, Y. Xie, M.P. Planche, H. Liao, G. Montavon, Microstructural evolution and mechanical properties enhancement of a cold-sprayed Cu-Zn alloy coating with friction stir processing, *Mater. Charact.* 125 (2017) 76–82, <https://doi.org/10.1016/j.matchar.2017.01.027>.
- [41] D. Xu, Z. Li, G. Wang, X. Li, X. Lv, Y. Zhang, Y. Fan, B. Xiong, Phase transformation and microstructure evolution of an ultra-high strength Al-Zn-Mg-Cu alloy during homogenization, *Mater. Charact.* 131 (2017) 285–297, <https://doi.org/10.1016/j.matchar.2017.07.011>.
- [42] J. Yuan, S. Pan, T. Zheng, X. Li, Nanoparticle promoted solution treatment by reducing segregation in AA7034, *Mater. Sci. Eng. A.* 822 (2021) 141691, <https://doi.org/10.1016/j.msea.2021.141691>.
- [43] C.L. Tai, Y.M. Pua, T.F. Chung, Y.L. Yang, H.R. Chen, C.Y. Chen, S.H. Wang, C. Y. Yu, J.R. Yang, The effect of minor addition of Mn in AA7075 Al-Zn-Mg-Cu aluminum alloys on microstructural evolution and mechanical properties in warm forming and paint baking processes, *Int. J. Light. Mater. Manuf.* 6 (2023) 521–533, <https://doi.org/10.1016/j.ijlmm.2023.04.001>.
- [44] J. Tang, Y. Yi, H. He, S. Huang, J. Zhang, F. Dong, Hot deformation behavior and microstructural evolution of the Al-Cu-Li alloy: A study with processing map, *J. Alloy. Compd.* 934 (2023) 167755, <https://doi.org/10.1016/j.jallcom.2022.167755>.
- [45] S. Gupta, R.S. Haridas, P. Agrawal, R.S. Mishra, K.J. Doherty, Influence of welding parameters on mechanical, microstructure, and corrosion behavior of friction stir welded Al 7017 alloy, *Mater. Sci. Eng. A.* 846 (2022) 143303, <https://doi.org/10.1016/j.msea.2022.143303>.
- [46] H. Xiong, Y. Zhou, P. Yang, C. Kong, H. Yu, Effects of cryorolling, room temperature rolling and aging treatment on mechanical and corrosion properties of 7050 aluminum alloy, *Mater. Sci. Eng. A.* 853 (2022) 143764, <https://doi.org/10.1016/j.msea.2022.143764>.
- [47] X. Qiu, N. ul H. Tariq, L. Qi, Y. ning Zan, Y. jiang Wang, J. qiang Wang, H. Du, T. ying Xiong, In-situ Sip/A380 alloy nano/micro composite formation through cold spray additive manufacturing and subsequent hot rolling treatment: Microstructure and mechanical properties, *J. Alloy. Compd.* 780 (2019) 597–606, <https://doi.org/10.1016/j.jallcom.2018.11.399>.
- [48] W. Zhao, L. Wang, Y. Ren, B. He, S. Han, P. Xu, Y. Liang, Effect of precipitates evolution on mechanical properties of Al 7050 alloy during secondary aging, *Mater. Res. Express* 10 (2023), <https://doi.org/10.1088/2053-1591/ace02b>.

- [49] N. Tian, X. Jiang, Y. Zhang, Z. Zeng, T. Wang, G. Zhao, G. Qin, Effect of Precipitates on the Mechanical Performance of 7005 Aluminum Alloy Plates, *Materials* 15 (2022), <https://doi.org/10.3390/ma15175951>.
- [50] J. Ren, R. Wang, C. Peng, Y. Feng, Multistage aging treatment influenced precipitate characteristics improve mechanical and corrosion properties in powder hot-extruded 7055 Al alloy, *Mater. Charact.* 170 (2020) 110683, <https://doi.org/10.1016/j.matchar.2020.110683>.
- [51] S. Pan, J. Yuan, C. Linsley, J. Liu, X. Li, Corrosion behavior of nano-treated AA7075 alloy with TiC and TiB₂ nanoparticles, *Corros. Sci.* 206 (2022) 110479, <https://doi.org/10.1016/j.corsci.2022.110479>.